Available online at www.sciencedirect.com

ScienceDirect

Journal of Magnesium and Alloys 9 (2021) 995–1006

www.elsevier.com/locate/jma

Effect of Ce-base mischmetal addition on the microstructure and mechanical properties of hot-rolled ZK60 alloy

E.P. Silva[a,b,*], R.H. Buzolin[c,d], F. Marques[b], F. Soldera[e], U. Alfaro[f], H.C. Pinto[b]

[a] *Institute of Engineering, Science and Technology (IECT), Federal University of Vales do Jequitinhonha e Mucuri (UFVJM), Janaúba, MG, Brazil*
[b] *São Carlos School of Engineering (EESC), University of São Paulo (USP), Department of Materials Engineering, CEP 13563-120 São Carlos-SP, Brazil*
[c] *Christian Doppler Laboratory for Design of high-performance alloys by thermomechanical processing, Kopernikusgasse 24/I, 8010 Graz, Austria*
[d] *Technische Universität Graz (TU Graz), Institute of Materials Science, Joining and Forming, Kopernikusgasse 24/I, 8010 Graz, Austria*
[e] *Institute of Functional Materials, Department of Materials Science and Engineering, Saarland University, Saarbruecken, Germany*
[f] *German Aerospace Center (DLR) Institute of Materials Research, Linder Höhe, 51147 Cologne, Germany*

Received 28 May 2020; received in revised form 8 September 2020; accepted 30 September 2020
Available online 5 November 2020

Abstract

Mg-Zn-Zr (ZK) alloys exhibit notably high mechanical strength amongst all magnesium alloy grades. However, due to the formation of low melting point Mg_3Zn_7-precipitates, these alloys are susceptible to hot cracking, thus compromising their metallurgical processing. The addition of rare earths to ZK alloys is an alternative to form higher melting point intermetallic compounds, speed up dynamic recrystallization, refine grain size, enhance corrosion resistance and extend the service temperature due to improved creep resistance. This work deals with the effect of Ce-base mischmetal addition on the hot rolling behaviour of as-cast ZK60 alloy. The microstructure investigation conducted using electron microscopy and X-Ray diffraction shows that precipitation of Mg_7Zn_3 intermetallics occur during hot rolling, whereas no further precipitation is observed for the ZK60-Mm alloys. The fragmentation of the intermetallic compounds occur during hot rolling and finer particles of Mg_7Zn_3 are observed for the ZK60, whereas Mg_7Zn_3 and $MgZn_2Ce$ intermetallics are formed in the alloy modified with mischmetal addition. A higher fraction of dynamically recrystallized grains is observed for the ZK60-Mm in comparison to the ZK60. Continuous recrystallization takes place in ZK60 with the formation of sub-grains near to the intermetallics and the addition of mischmetal promotes the occurrence of discontinuous recrystallization with the nucleation of new grains close to the precipitates. The mechanical strength and, in particular, the ductility of the hot-rolled alloys are notably improved when compared to the same alloys in the as-cast condition. The mechanical strength is, however, higher for the ZK60 alloy. Less solid solution strengthening, softer $MgZn_2Ce$ intermetallics and more extensive recrystallization contribute to reduce the mechanical strength of ZK60-Mm. Failure in both alloys are initiated at coarse intermetallics and propagate through intermetallic-rich regions.

Keywords: Magnesium alloys; Hot rolling; Mischmetal; Recrystallization; Microstructure; Mechanical properties.

1. Introduction

The growing scarcity of renewable energy resources requires a dramatic reduction in energy used for transportation. An alternative to diminish the energy consumption is the reduction of structural weight by using light alloys, such as magnesium-base materials. Mg alloys are of great interest for a variety of challenging applications which demand distinguished mechanical performance, thermal conductivity and damping capability [1]. Cost control is also of great technological relevance to pursue low cost but high performance Mg alloys [2]. In this regard, ZK60 (Mg-6.0Zn-0.6Zr (wt.%)) alloy offers a good compromise between high strength, ductility, and low manufacturing costs.

* Corresponding author at: Federal University of Vales do Jequitinhonha e Mucuri (UFVJM), Institute of Engineering, Science and Technology (IECT), Avenida Um, n° 4.050. Cidade Univ…, 39447-814 Janaúba, MG, Brazil.
E-mail address: erenilton.silva@ufvjm.edu.br (E.P. Silva).

https://doi.org/10.1016/j.jma.2020.09.018

Investigations regarding the effect of rare earths (RE) on Mg alloys is extensive. The influence of rare earths on the mechanical properties and corrosion behaviour [3] of Mg-Al alloy system has been reported. Mg alloys with RE addition show potential for achieving improved strength and creep resistance compared with the AZ system and the most notable alloys are based on the Mg-Gd, Mg-Gd-Y, Mg-Gd-Nd, and Mg-Y-Nd systems [4–7]. Rare earths also notably enhance the strength and creep resistance of Mg alloys [4–8]. The addition of lanthanides, Sc and Y to the Mg-Zn-Zr alloys modify their microstructure leading to enhanced room temperature mechanical strength [9]. Moreover, castability [10] as well as elevated temperature strength [11] can be improved owing to the constitutional supercooling and thereby grain refinement [12], which lead to enhanced ductility at room temperature [13,14]. The formation of a discontinuous network of RE-containing intermetallics along the grain boundaries has been also reported to improve the mechanical strength at room and high temperatures [11].

Conventional Mg alloys usually exhibit poor formability at room temperature [15], mainly due to the limited number of slip systems available and twinning play a major role as deformation mechanism. Forming, therefore, is normally conducted at temperatures above 225 °C where the activation of the non-basal slip system occurs, facilitating dislocation slip, improving the formability [16]. Furthermore, RE addition weakens the basal texture (<0001> // ND) in wrought alloys [17–25], thus material formability can be notably enhanced [26]. The orientation spread of the basal planes is broader towards the sheet transverse direction (TD) and recrystallization appears as the main mechanism causing weak texture in RE-containing wrought Mg alloys.

Due to the high costs associated with RE alloying, mixtures of rare earths, such as Ce-base Mischmetal (Ce-Mm), are an attractive alternative. Cerium is the main constituent of the Ce-Mm with a typical weight fraction of ~ 50–75%, followed by lanthanum as the second main chemical element. The addition of Mm lead to the formation of intermetallics that can be fragmented into finer particles during hot rolling, and act as nucleation sites for recrystallization, thus playing an important role as particle-stimulated nucleation (PSN) [26].

The aim of this work is hence to clarify the influence of Ce-base Mischmetal on the hot rolling behaviour of ZK60 alloy regarding the microstructure formation and the resulting mechanical properties at room temperature.

2. Experimental

2.1. Materials and processing

Two as-cast Mg alloys, named as ZK60 (Mg-6.0Zn-0.6Zr (wt.%)) and ZK60-Mm (Mg-6.0Zn-0.6Zr-1.5Mm (wt.%)), were hot rolled at 315 °C and 345 °C, respectively [26]. Ce-base mischmetal used to cast the ZK60-Mm alloy had the following chemical composition: 55% wt. Ce, 24% wt. La, 16% wt. Nd, 5% wt. Pr. The initial thickness of the plates for ZK60 and ZK60-Mm were 15 mm and 17.65 mm, respectively. Passes of 2.5% were performed up to a strain of 50%, followed by two final passes of 15%, thus reaching a total strain of 65%. Initially, the plates were homogenized at the rolling temperature for 30 min. An inter-pass annealing of 20 min was conducted and immediately after the last pass the plates were water quenched. The hot rolling process was conducted in normal atmosphere.

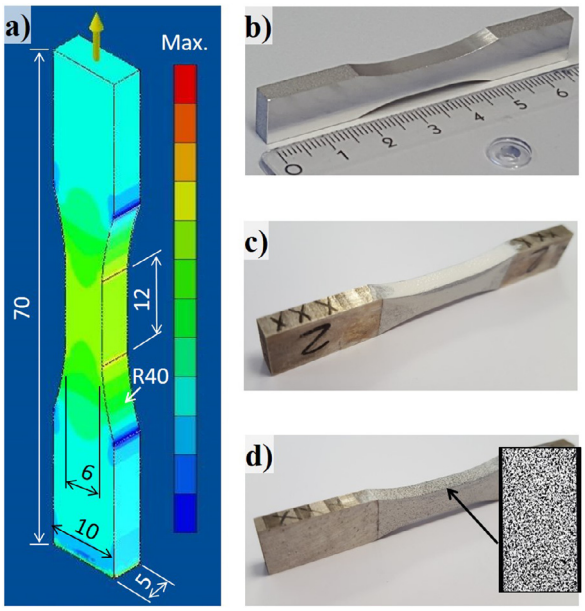

Fig. 1. Tensile specimens: a) software simulation and dimensioning according to ASTM E8M, b) specimen after machining, c) specimen with a layer of white AQUA lack and d) specimen with final preparation and detailing the surface where fine graphite particles were sprayed for strain determination.

Samples from the transversal direction (TD) and rolling direction (RD) were cut from the rolled plates. Conventional metallography was carried out by grinding using SiC papers from grid 800 to grid 4000. The specimens were polished afterwards using an OPS suspension and 1 μm diamond solution, followed by a final polishing step of ~20 s using OPS suspension.

2.2. Material characterization

Tensile testing was performed using a TesTWinner 922, TesT GmbH, Germany. A strain rate of 0.074 mm/min was used. Local deformation analysis was carried through the NIKON D7000 camera and the data was analysed by the ARAMIS software. An image acquisition of one every 10 s was used during tensile testing. Fig. 1 displays the size and shape of tensile specimens.

Fractography and microstructural analysis were performed using a FEI Inspect FL50, ThermoFisher, USA and an Ultra 55, ZEISS GmbH, Germany scanning electron microscopes (SEM) equipped with a field emission gun (FEG-SEM), an Oxford Electron Backscattered Diffraction (EBSD) detector and an Energy Dispersive X-Ray Spectroscopy (EDXS) system. The accelerating voltage was 15 kV and the EBSD results

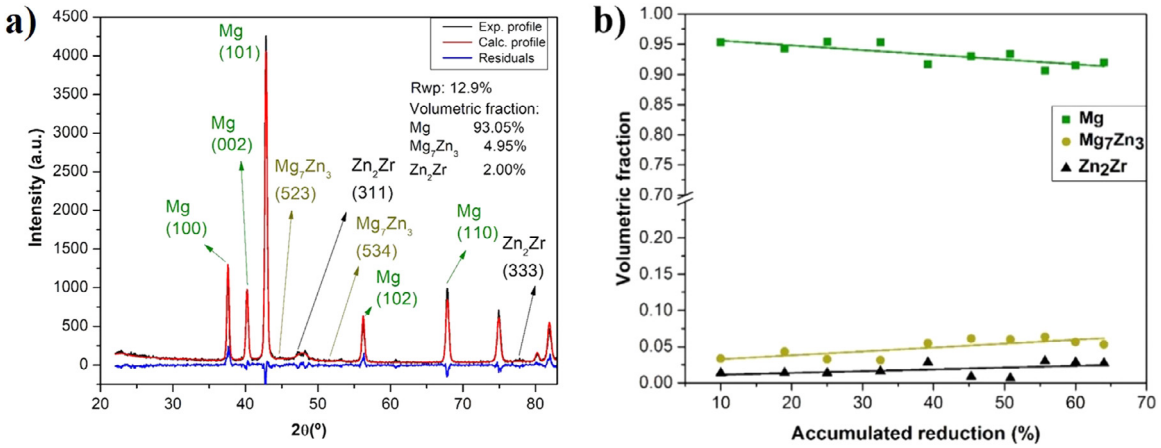

Fig. 2. Phase identification for the ZK60 alloy: a) Diffractogram after the second pass after rolling with the indicated phases and crystallographic planes as well as the result of the Rietveld refinement; b) evolution of phase volume fractions during hot rolling with respect to the accumulated reduction.

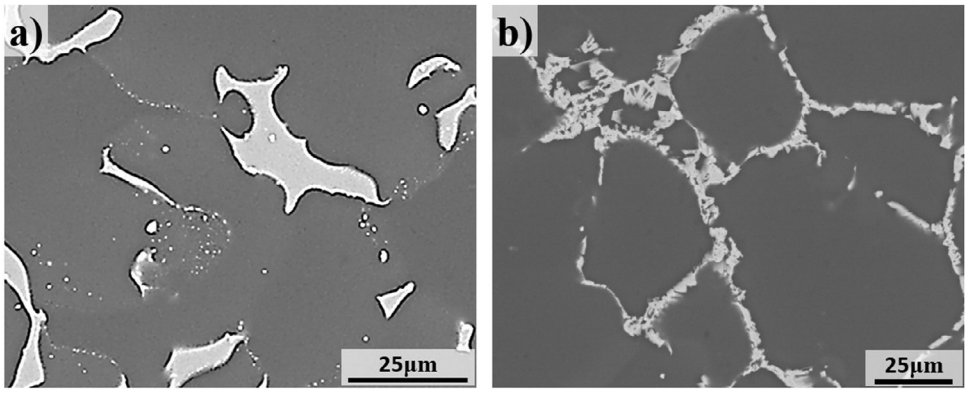

Fig. 3. SEM-SE micrographs of the alloys after 30 min homogenization at the rolling temperature: a) as-cast ZK60 and b) as-cast ZK60-Mm.

were evaluated using Oxford's Channel 5 software, Oxford instruments, UK.

X-ray diffraction (XRD) was conducted using a PANalytical MRD-XL diffractometer, Malvern Panalytical, UK, with Co-Kα radiation. The diffractograms were measured in the 2θ interval from 5° to 100° with a step of 0.05° The acquisition time of 10 s and a beam of 4×4 mm^2 were used. The tested specimens were extracted from the plates after every rolling pass to evaluate the phase and microstructure evolution during hot-rolling.

MAUD® software [27] was used for Rietveld refinement of measured X-ray diffractograms after each rolling pass on the sample cross-sections perpendicular to the rolling direction (RD). α-Mg, Mg_7Zn_3 [28], $MgZn_2Ce$ and Zn_2Zr [26] were the considered indexed phases. The anisotropic Popa model [29] was used for the determination of crystallite size and microstrain. March-Dollase model [30] was applied to simulate the texture components along the RD. Furthermore, the full width at half maximum (FWHM) was determined for the diffraction lines of the basal, prismatic and pyramidal lattice planes using the software PeakFit®. The FWHM values were additionally normalized with respect to their maximum value for each investigated alloy.

3. Results and discussion

3.1. Microstructure

Figs. 2 and 4 show the diffractograms obtained in the RD direction of the rolled plates and the phase volume fractions obtained from the Rietveld refinements for the ZK60 and the ZK60-Mm, respectively. A selected Rietveld refinement for the ZK60 alloy is shown in Fig. 2a and the measured phase fractions are: 93,07% of α-Mg, 4,95% of Mg_7Zn_3 and 1,98% of Zn_2Zr. In addition, Fig. 2b shows the evolution of phase fractions for different accumulated reductions. The increase in volume fraction of the Zn-containing intermetallic compounds in ZK60 is attributed to the simultaneous formation and growth of the present intermetallic compounds in the as-cast microstructure. That process is attributed to the existence of zones of supersaturated solid solution (SSSS) in the as-cast microstructure after homogenization, promoting growth of the already present intermetallic compounds due to Zn intake as well as the nucleation and growth of new intermetallic compound particles. The homogenization and solution treatments for ZK60 alloys were shown to be incomplete in [31–32]. Fig. 3 compares the microstructures of ZK60

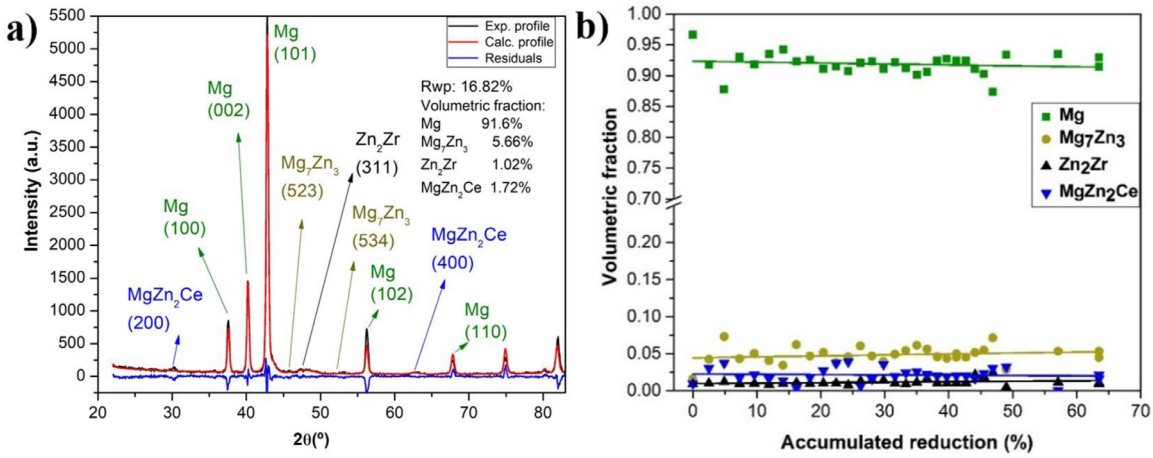

Fig. 4. Phase identification for ZK60-Mm alloy: a) Diffractogram after the second pass after rolling with the indicated phases and crystallographic planes as well as the result of the Rietveld refinement; b) evolution of phase volume fractions during hot rolling with respect to the accumulated reduction.

and ZK60-Mm after 30 min homogenization at the rolling temperature.

Fig. 4a illustrates a selected Rietveld refinement for ZK60-Mm, and after the second rolling pass, the identified phases and measured volume fractions are: 91.60% of α-Mg, 5.66% of Mg_7Zn_3, 1.72% of $MgZn_2Ce$ and 1.02% of Zn_2Zr. Fig. 4b exhibits the phase evolution during hot rolling, obtained from the Rietveld refinements. There is no notable change in volume fraction for the identified phases, indicating that there is no SSSS region in the as-cast microstructure of the ZK60 alloy modified with mischmetal that can promote the coarsening of the intermetallic compounds or nucleation and growth of new particles. Fig. 3b corroborates that the α-Mg matrix in ZK60-Mm is not supersaturated after 30 min homogenization. Both, the formation of stable intermetallic compounds at the rolling temperature and lower Zn content within the α-Mg matrix due to the Zn intake to form intermetallic compounds containing cerium, can explain the negligible change in phase fraction for the ZK60-Mm alloy. It also indicates that at 345 °C there is no dissolution of intermetallic compounds for ZK60-Mm owing to the higher formation temperature of the RE-containing intermetallics, thus revealing a more thermally stable microstructure in comparison to ZK60.

Figs. 5 and 6 shows the microstructure of the as-cast ZK60 and ZK60-Mm alloys, respectively. ZK60 exhibits a grain size of ~150 μm and ZK60-Mm of ~125 μm [34]. As shown in Fig. 5 (EDS spot analyses), ZK60 exhibits a continuous network of intermetallic compounds of Mg_7Zn_3 along the grain boundaries. The network of intermetallic compounds is mainly located along the grain boundaries and also partially distributed along the dendritic arms, consisting of a typical as-cast microstructure. In addition, disperse Zn_2Zr particles are observed within the α-Mg matrix, as shown in Fig. 5 and indicated on the EDS line scan, whereas chemical segregations are observed within the ZK60 grains. Higher concentration of solid solution elements is verified in the vicinity of the intermetallic compounds as a result of the segregation of heavy substitutional elements during accelerated solidification that is caused by Permanent Mould Indirect Chill Casting (PMICC) with a progressive immersion of the crucible into a reservoir containing water at room temperature [33,34]. The regions with higher concentration of alloying elements within solid solution are the source of Zn and Zr for the coarsening or precipitation of intermetallic compounds during hot rolling, in agreement with the increasing volume fraction of the intermetallic compounds in ZK60 verified in the XRD analyses, Fig. 2b.

The formation of low melting point intermetallic compounds in Mg-Zn-Zr and Mg-Zn-RE alloys is well-known [35]. The addition of RE to the ZK magnesium alloys promotes the formation of a larger volume fraction of intermetallic compounds due to the high chemical affinity between Zn, Zr and RE elements [36]. The typical microstructure of ZK60-Mm is shown in Fig. 6. A denser network of intermetallic compounds along the grain boundaries is observed and the chemical segregation of solid solution elements is less pronounced in comparison to the ZK60 alloy (Fig. 3b). The major intermetallic phase is $MgZn_2Ce$ and smaller volume fractions of discrete Mg_7Zn_3 and Zn_2Zr particles are present. The distribution of the chemical elements present in the alloy can be seen in the EDS maps shown in Fig. 6.

Fig. 7 shows the typical hot-rolled microstructure of the investigated alloys after 65% reduction. In both, ZK60 and ZK60-Mm alloys, the intermetallic compounds were elongated along the rolling direction and compressed along the normal direction, indicating they also deformed plastically during rolling. The intermetallic compounds are harder than the α-Mg matrix, thus plastic strain is concentrated within the α-Mg matrix. Additionally, the intermetallic compounds in the ZK60 alloy appear orientated nearly parallel to the rolling direction, while the network of intermetallic compounds was less modified in the of ZK60-Mm alloy. This indicates that the increased intermetallic fraction verified in the ZK60-Mm alloy is able to hamper the reorientation of the intermetallic network during hot working.

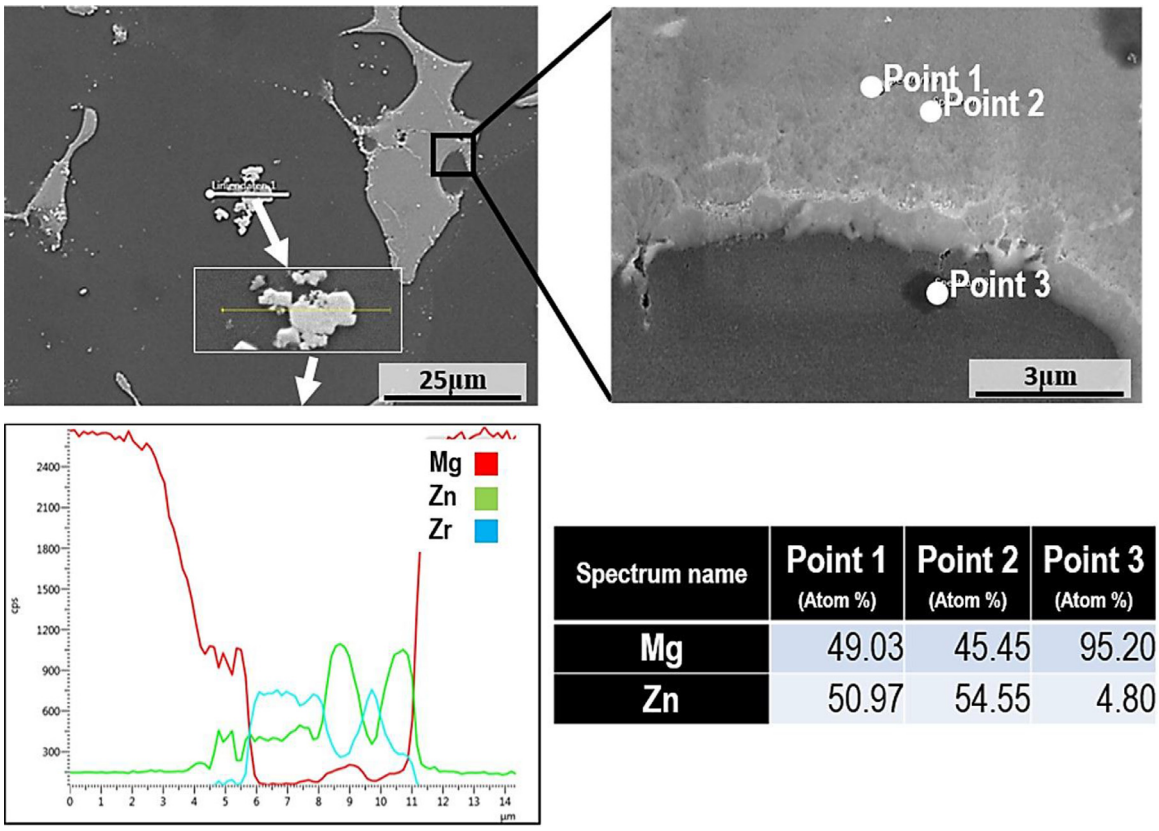

Spectrum name	Point 1 (Atom %)	Point 2 (Atom %)	Point 3 (Atom %)
Mg	49.03	45.45	95.20
Zn	50.97	54.55	4.80

Fig. 5. SEM-SE micrographs of the as-cast ZK60 alloy with EDS line scan and spot analyses to identify intermetallics.

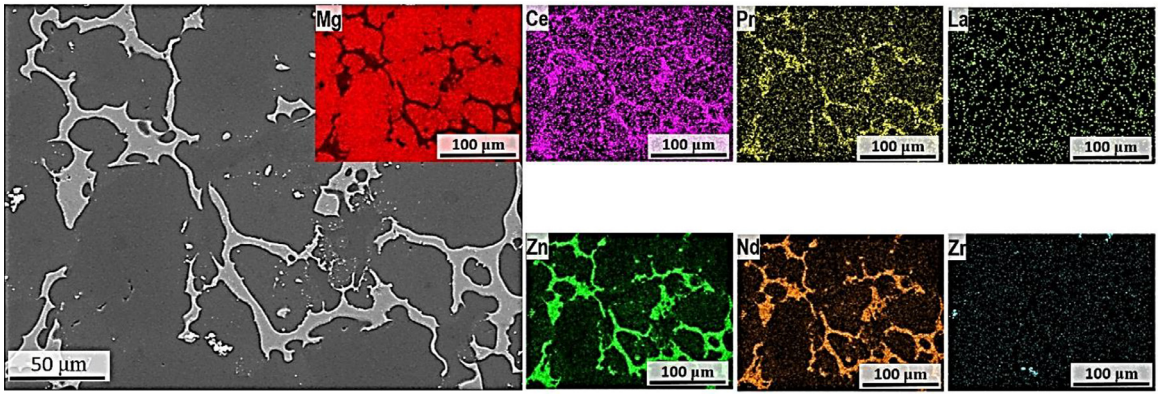

Fig. 6. SEM-SE micrographs of the as-cast ZK60-Mm alloy with EDS maps to identify intermetallics.

As a further result of plastic deformation, the intermetallic compounds of ZK60 were fragmented into small particles of ~1–2 µm, Fig. 7b. Additionally, small precipitates grown in the vicinity of grain boundaries are also observed. In contrast, the increased fraction of precipitates in ZK60-Mm hinders the fragmentation of the intermetallic network, thus causing the occurrence of larger particles of ~5 µm, Fig. 7d. Moreover, fine intermetallics do not grow near the grain boundaries after hot rolling of the ZK60-Mm alloy, thus corroborating the XRD results that suggest the absence of SSSS after adding mischmetal. Micro-cracks are also initiated in the ZK60-Mm alloy through the intermetallics and along the interface with the α-Mg matrix. Thus, the micro-cracks are a result of higher stress peaks that occur in ZK60-Mm owing to its more extensive and partially continuous network of intermetallics as well as its coarser size of precipitates and low ductility.

The broadening of a diffraction line is caused by the combination of the effects of crystallite size and micro-strains associated to structural defects, such as solute atoms, stacking faults and dislocations [37]. The increase in peak broadening is caused by the reduction in crystallite size and/or increase of micro-strains into the lattice structure [38,39]. Therefore, the evolution of the full width at half maximum (FWHM) of the diffraction lines can be used as a qualitative parameter to

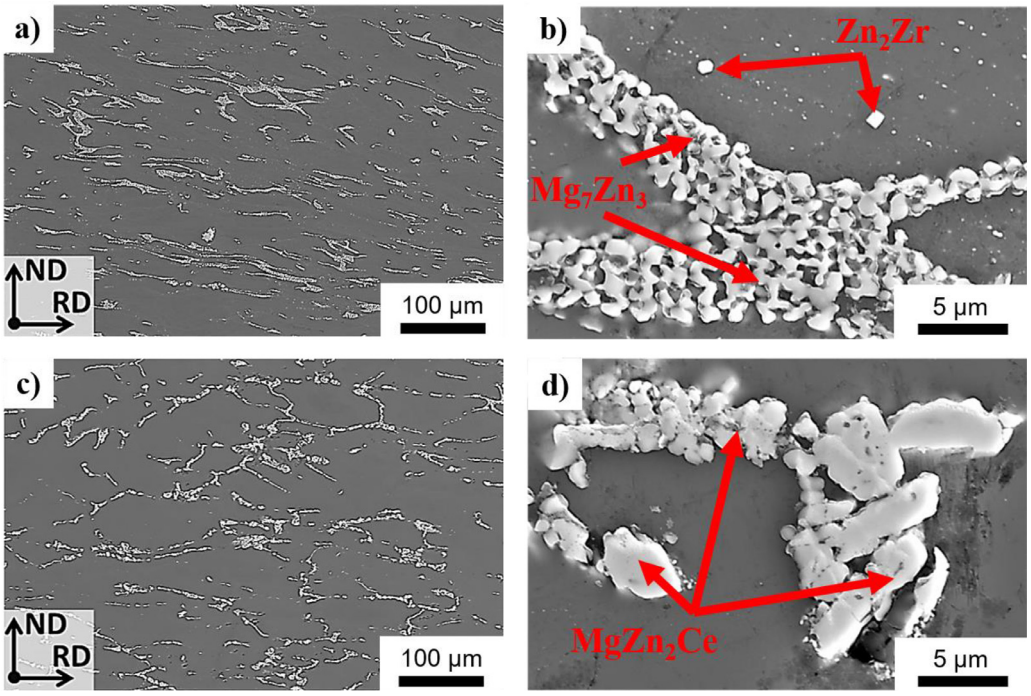

Fig. 7. SEM-SE micrographs of the hot-rolled alloys after 65% reduction: a,b) ZK60; c,d) ZK60-Mm.

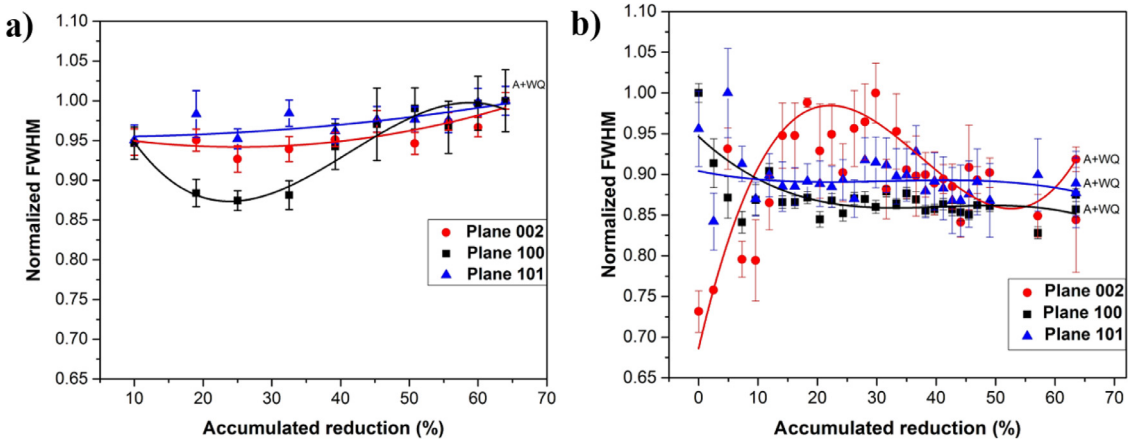

Fig. 8. Normalized FWHM as a function of the accumulated reduction during hot rolling for: a) ZK60; b) ZK60-Mm.

accompany the microstructure evolution during hot rolling. In addition, Moore e Evans [40] also showed that the FWHM can indirectly be correlated to the stored energy in the material due to plastic deformation [40–43].

Fig. 8 shows the evolution of the normalized FWHM of the diffraction lines coming from basal, prismatic and pyramidal lattice planes with respect to the accumulated deformation during hot rolling. Higher values of FWHM are observed for the ZK60, Fig. 8a. Moreover, the values mostly increase with increasing accumulated deformation, although an initial reduction of FWHM is verified for the (100) diffraction line. This slight decrease in FWHM during the first rolling steps of ZK60 is related to the removal of Zn solute from the supersaturated α-Mg matrix, which causes decreasing lattice distortion and further precipitation of Mg_7Zn_3 intermetallics with increasing rolling steps, as revealed by the Rietveld analyses in Fig. 2b. For the ZK60-Mm the values of FWHM for the basal plane (002) increase only during the initial passes, Fig. 8b, whereas for the diffraction lines of prismatic and pyramidal lattice planes a continuous decrease of FWHM is verified. The steep increase in FWHM during the first rolling steps of ZK60-Mm is attributed to increasing lattice defects, such as dislocations, twins and stacking faults that demand longer exposure to the rolling temperature to be fully restored.

Starting from an as-cast microstructure, the increase in dislocation density associated with the rapid work hardening increases the stored energy in the material. At high temperatures, the occurrence of dynamic recovery can lead to a saturation at the stored energy. However, for materials with low to intermediate stacking fault energy, such as magnesium

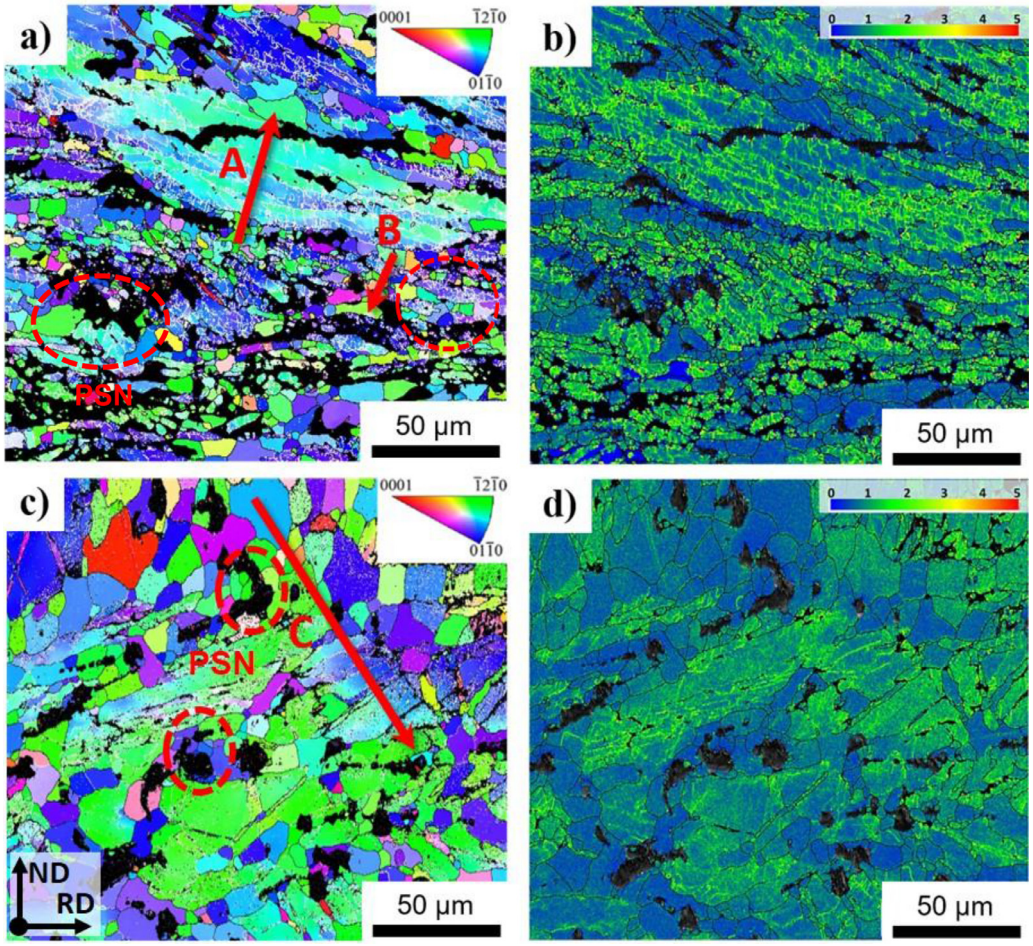

Fig. 9. Inverse pole figure (IPF) maps for the α-Mg matrix of the hot-rolled alloys: a) ZK60; c) ZK60-Mm. Boundaries of misorientation angle $> 15°$ are marked in black and between 2° and 15° in white. The arrows "A", "B" and "C" indicate profiles of misorientation angle that are shown in Fig. 7. Kernel Average Misorientation (KAM) maps for the hot-rolled alloys: b) ZK60; d) ZK60-Mm.

alloys, the role of dynamic recovery is less pronounced in comparison to metallic alloys with high stacking fault energy [44], thus an increase in stored energy with increase in deformation can be observed. At high temperatures, continuous and/or discontinuous dynamic recrystallization can occur, reducing the stored energy in the material [45]. Additionally, twinning and stacking fault formation can take place in magnesium and its alloys, thus contributing to the increase in stored energy [46]. Static recovery and static recrystallization are also active restoration mechanisms during annealing, such as for the inter-passes during the rolling of the investigated alloy. Therefore, for the ZK60 alloy, the progressive increase in FHWM with ongoing rolling steps can be correlated to the progressive increase in stored energy with the accumulated rolling reduction. On the other hand, for the ZK60-Mm, the initial increase followed by a slightly decrease in FWHM can indicate the occurrence of dynamic recrystallization during deformation as well as static recrystallization during the inter-passes annealing for this alloy as restoration mechanisms reducing the stored energy.

Figs. 9(a,c) exhibit the inverse pole figures (IPF) maps for the ZK60 and ZK60-Mm, respectively. The microstructure is notably heterogeneous, with regions of fine grains in the vicinity of the intermetallic compounds and regions with high misorientation spreading within larger grains. The black boundaries indicate the high angle grain boundaries (misorientation angle $> 15°$) while the white boundaries, the low angle grain boundaries (misorientation angle $< 15°$). For the ZK60 the density of low angle grain boundaries is larger compared with the ZK60-Mm. Moreover, the amount of fine grains in the vicinity of the intermetallic compounds is larger for the ZK60 compared with the ZK60-Mm.

Additionally, Figs. 9(b,d) show the Kernel Average Misorientation Angle (KAM) maps for the ZK60 and ZK60-Mm, respectively. The density of the low angle grain boundaries and their level or organization can be inferred by a KAM map. Well-organized low angle grain boundaries can be observed as sharp KAM boundaries, while a more diffuse distribution of KAM in a low angle grain boundary indicates a more disorganized arrangement of dislocations forming the low angle grain boundary. The level of organization of a subgrain boundary can also be correlated to the role of recovery. If the dislocations can be easily rearranged into sharp low angle grain boundaries, an extended role of recovery can be

inferred. Therefore, KAM indicates qualitatively the stored energy in a microstructure. Higher values of KAM correspond to higher stored energy. ZK60 exhibits a heterogenous distribution of KAM, where zones of fine sub-grains as well as deformed and elongated magnesium grains. On the other hand, the density of KAM for the ZK60-Mm is smaller and is more homogeneous distributed, indicating that the role of recrystallization on the microstructure formation is more pronounced for the ZK60-Mm in comparison to the ZK60.

During hot working [47], discontinuous dynamic recrystallization is frequently observed for materials with low stacking fault energy, where the nucleation of new strain-free grains takes place and the recrystallized nuclei grow at the expense of distorted regions with high dislocation densities. Cell or sub-grain structures associated with the formation of low angle grain boundaries are verified during deformation of materials with high stacking fault energy due to the elevated mobility of screw dislocations and therefore efficient dynamic recovery. Those sub-grain structures progressively evolve into high angle grain boundaries at larger deformations, thus characterizing the so-called continuous dynamic recrystallization.

Particle stimulated nucleation (PSN) of recrystallization nuclei appears as an important restoration mechanism in both alloys, as indicated by red dashed circles in Figs. 9(a,c). However, continuous recrystallization seems to occur in ZK60 with the polygonization of dislocation structures near to the intermetallics (non-indexed areas). In ZK60-Mm small new grains are nucleated close to the precipitates indicating the occurrence of discontinuous recrystallization.

The presence of grains with low misorientation spread and low density of low angle grain boundaries suggest that they were formed by recrystallization, either static or dynamic. In the case of hot rolling process applied to the investigated alloys, the static recrystallization can occur during the interpass annealing and the dynamic recrystallization during hot rolling. Fig. 10 shows the misorientation angle profile with respect to the point of origin for the indicated lines “A”, “B” and “C” in Fig. 9(a,c). The high angle grain boundaries are indicated by the blue arrows while the low angle grain boundary by the green ones. Additionally, grains with large misorientation spread are indicated by the dashed black ellipses. The formation of low angle grain boundaries shows that recovery played an important role during the hot rolling of the investigated alloys. In Fig. 10a the misorientation angle between sub-grains is in the range of 5–10° as indicated by the green arrows. The misorientation spread observed within a grain and sub-grains indicate that the produced dislocations did not have sufficient time to be reorganized into sharp low angle grain boundaries.

Therefore, the misorientation angle profile for the ZK60 alloy (Fig. 10(a,b)) exhibits two clearly different tendencies:

I: regions with notable low misorientation angle spread within a grain and with a large misorientation angle with respect to the neighbouring grains;
II: regions with large misorientation angle spread.

Region I corresponds to a recrystallized microstructure formed during the process, while region II is related to a deformed microstructure where the low angle grain boundaries are formed via static or dynamic recovery. ZK60 and ZK60-Mm exhibit both regions and it is notable that region I is located in the vicinity of intermetallic compounds, while region II is located within the grains, especially within large ones. The volume region of region I is higher for the ZK60-Mm compared with the ZK60. The higher rolling temperature promotes increase the mobility of high angle grain boundaries as well as the recrystallization kinetics, either static or dynamic. The formation of a substructure due to recovery as indicated in region II shows a partially recrystallized microstructure. The stored energy for recrystallization is the dislocation density accumulated during deformation. Higher temperatures lead to higher activity of recovery, as well as it promotes recrystallization. Therefore, the higher temperatures of rolling for the ZK60-Mm seem to have promoted recrystallization, either static and/or dynamic. However, it is not possible to distinguish between static and dynamic recrystallization in the observed microstructure. Moreover, the progressive increase in boundary misorientation during hot deformation [48] as the main mechanism of continuous dynamic recrystallization [49]. are also reported to occur during hot rolling of ZK60 [50]. However, the heterogeneous distribution of stresses [51] and the limited role of dynamic recovery [52] limits the occurrence of continuous dynamic recrystallization during hot deformation, and its role seem not to be pronounced for the investigated alloys.

The misorientation angle notably higher than 15° indicates that those boundaries are either already existing high angle grain boundaries prior to deformation, or they are formed due to static [51], discontinuous dynamic recrystallization [53] or continuous dynamic recrystallization [49]. The presence of recrystallized regions in the vicinity of the intermetallic compounds suggests that the production and pile-up of dislocations are higher in those regions during deformation and can be attributed due to the load partitioning between intermetallic compound and α-Mg matrix. Moreover, the dislocation multiplication is larger in the vicinity of the grain boundaries [54], as well as in the softer phase in the vicinity of interfaces with a harder phase [55] increasing the dislocation densities in those regions. Therefore, the accumulation of dislocations in the vicinity of intermetallic compounds can lead to particle-stimulated nucleation, as reported for Mg-Mn alloys [56] and other Mg alloys [57,58].

3.2. Mechanical properties

The mechanical properties of the hot-rolled alloys at room temperate were assessed by tensile testing, as shown in Fig. 11. The ZK60 alloy exhibits superior properties in comparison to the ZK60-Mm alloy, with a maximum strength ~11% higher and a yield stress ~ 26% higher than the ZK60-Mm. The mechanical properties for each alloy are listed in Table 1. The yield stress values of ZK60 and ZK60-Mm are 269 and 199 MPa, respectively, and ~ 43% higher than those

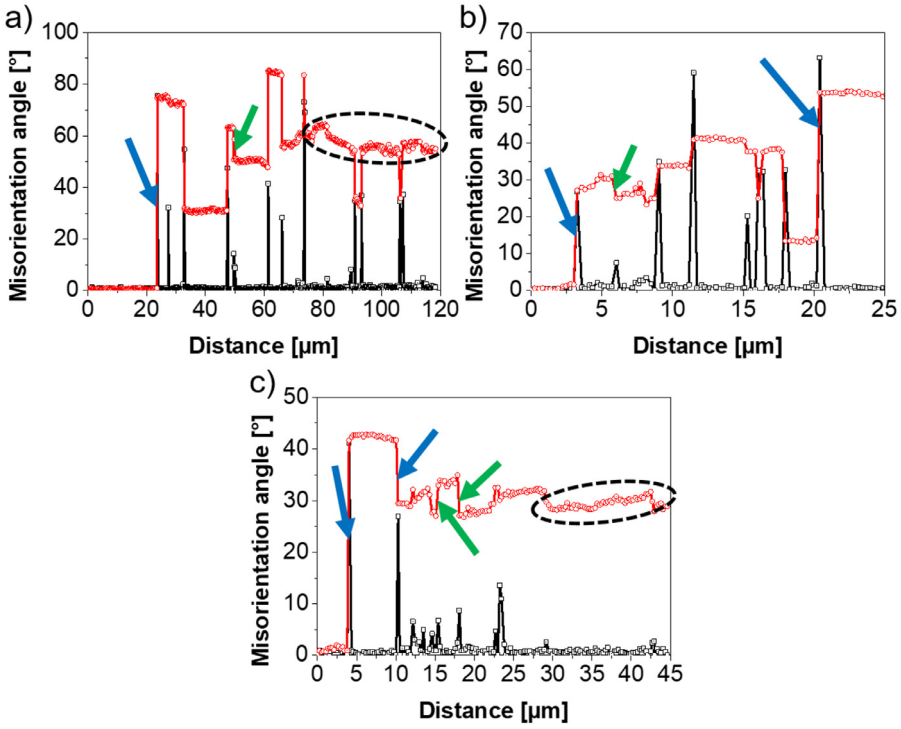

Fig. 10. Misorientation angle profiles highlighted in Fig. 6 for: a,b) ZK60 and c) ZK60-Mm. Blue and green arrows indicate the high and low angle grain boundaries, respectively. The dashed black ellipses indicate a grain/sub-grain with notable misorientation spread.

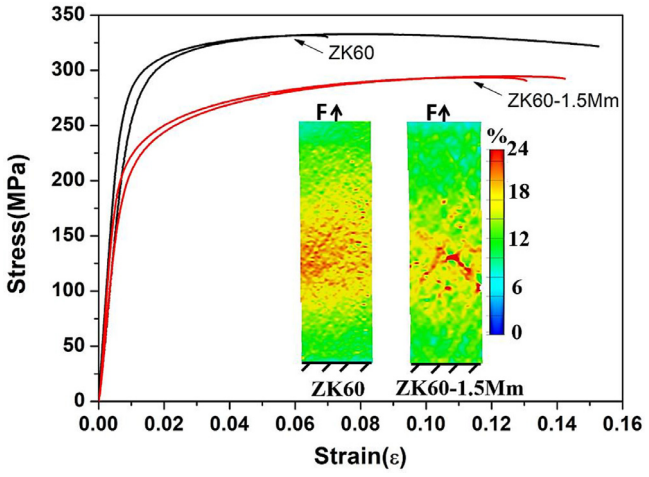

Fig. 11. Engineering stress vs. strain curves of the hot-rolled alloys, obtained by room temperature tensile tests with local deformation analysis carried out using the ARAMIS software.

Table 1
Mechanical properties obtained from the tensile testing of the hot-rolled alloys.

Material	σ_{max} (MPa)	σ_r (MPa)	σ_e (MPa)	Elongation (%)
ZK60	332	326	269	10.1
ZK60-Mm	294	292	199	11.5

exhibited for the same alloys in the as-cast condition [34]. Hot rolling of the investigated alloys also increased their elongation to fracture, in particular for the ZK60-Mm alloy, with an elongation of 11.5%, which is approximately 82% higher than that exhibited for the same alloy in the as-cast condition [34].

The mechanical behaviour of the hot-rolled alloy with mischmetal addition is not obvious and can be attributed to different issues. First, the solid solution strengthening of the α-Mg matrix diminishes since the mischmetal causes the precipitation of $MgZn_2Ce$ intermetallics, thus removing Zn from solid solution. Second, it was verified in [34] that Mg_7Zn_3 precipitates are harder than $MgZn_2Ce$. Finally, XRD analyses revealed that ZK60 undergoes strain hardening during hot rolling, whereas recrystallization is expressive for ZK60-Mm, thus leading to material softening. Those mechanisms promote therefore lower mechanical strength and enhanced ductility in the ZK60-Mm alloy. Despite lower mechanical strength, $MgZn_2Ce$ intermetallics have higher melting point than Mg_7Zn_3. Along with a better ductility, this implies in a better hot workability and weldability of ZK60-Mm if compared to ZK60.

The simulated cross-sectional images of tensile specimens using the Aramis software shows the strain distribution at the maximum strength of each hot-rolled alloy, as shown in the inserts in Fig. 11. The strain concentration is more pronounced for the ZK60-Mm alloy in comparison to the ZK60 alloy. This contributes to decrease the maximum strength achived for the ZK60-Mm alloy. The occurrence of a coarser size of broken intermetallics after hot rolling, as verified in Fig. 7d, as well as the more extensive and partially continuous network of precipitates in ZK60-Mm leads to the localization of deformation, which thus nucleate earlier cracks within the

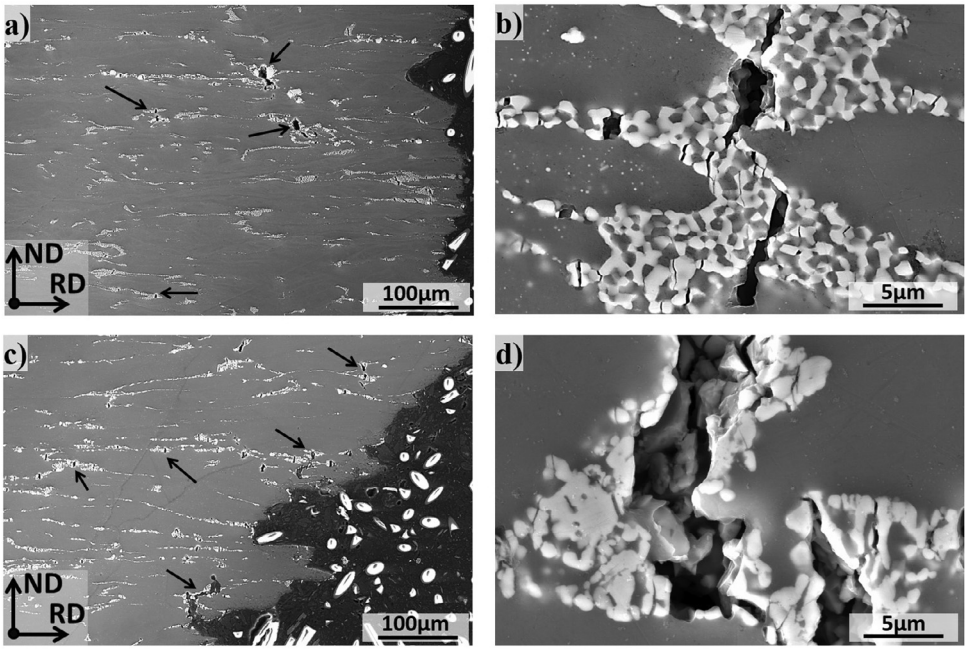

Fig. 12. Secondary electrons (SEM-SE) images of the cross section of the fractured specimens after tensile testing: a), b) ZK60; c), d) ZK60-Mm.

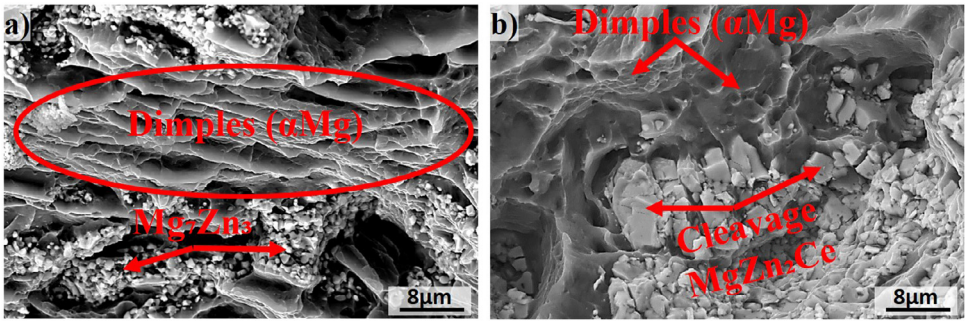

Fig. 13. Secondary electrons (SEM-SE) images of the fracture surface of the rolled alloy after tensile testing; a) ZK60 and b) ZK60-Mm.

intermetallic compounds and at their interfaces with the α-Mg matrix and slightly decrease the mechanical strength, as already observed for the castings [34].

Fig. 12 shows that in both alloys the fracture propagated through the network of the intermetallic compounds, and started at the interfaces between intermetallics and with the α-Mg matrix, as shown in Fig. 12 (b,d). The smaller and better distributed the intermetallic particles are, the lower the strain concentration and the lower the probability to nucleate and grow a micro-crack through the intermetallic compounds. Hence, a more continuous network of intermetallic compounds along with greater strain concentration speed up the crack propagation across the ZK60-Mm alloy, thus causing its embrittlement in despite of having lower mechanical strength.

Fig. 13 shows the fracture surfaces of the tensile tested specimens. The ZK60 alloy, Fig. 13a, presents a more ductile type of fracture with the formation of dimples, in this case at an angle of 40° to 50° with respect to the fractured surface. Regions with intermetallic particles are also present. The precipitates appear once again on the fracture surfaces clearly finer in ZK60 than in the alloy with mischmetal addition. A mixed fracture profile is observed for the ZK60-Mm alloy, Fig. 12b. Ductile fracture with the formation of dimples is observed within the α-Mg matrix, whereas brittle fracture via cleavage is verified along the coarser intermetallic compounds in ZK60-Mm.

4. Conclusions

The present work dealt with the effect of Ce-base mischmetal addition on the microstructure formation and the resulting mechanical properties of hot-rolled ZK60 alloy at room temperature. Scanning electron microscopy coupled with electron backscattered diffraction, X-ray diffraction, Rietveld simulations and tensile testing combined with image correlation allowed to draw the following conclusions:

- The proposed hot rolling routes allowed for the complete modification of the solidification microstructure in both alloys and promoted much better mechanical strength and elongation to fracture in comparison to the castings.

- The addition of Ce-base mischmetal led to increased recrystallized fractions in the ZK60-Mm alloy and particle stimulated nucleation of recrystallization nuclei appear as an important restoration mechanism. Under the hot rolling conditions investigated, discontinuous recrystallization seems to take place in ZK60-Mm, whereas continuous recrystallization appears to be the main restoration mechanism in ZK60 with the formation of small sub-grains close to the intermetallics. However, further investigations are required to systematically accompany the evolution of restoration mechanisms as a function of the strain rate and to determine more precisely the role of the alloying elements and precipitates in the dynamic restoration processes.
- Less solid solution strengthening, softer $MgZn_2Ce$ intermetallics and more extensive recrystallization caused lower mechanical strength and increased ductility in the ZK60-Mm alloy.
- Strain concentration and embrittlement are more pronounced after mischmetal addition in despite of lower mechanical strength owing to the formation of coarser precipitates after hot rolling and the existence of a partially continuous network of intermetallics.
- During tensile testing, cracking initiates in the regions with coarser precipitates and propagates throughout intermetallic-rich zones.

Acknowledgements

The authors acknowledge the funding of FAPESP, processes 2010/11391-2, 2011/09324-8 and 2011/19218-0. The authors are also thankful to the RIMA Group for supplying the raw materials used in the production of magnesium alloy castings. In addition, EPS acknowledges FAPESP and CNPQ for the scholarships. HP is CNPq fellow. HP and FS thank the funding provided by CAPES (PROBRAL project 88881.143948/2017-01). The German Aerospace center (DLR) is greatly acknowledged for providing access to the EBSD facility and the digital image correlation tool for mechanical tensile testing.

References

[1] K.U. Kainer, Magnesium alloys and technology, Wiley-CVH Gmbh & Co. KGaA, Weinheim, 2003.
[2] S.M. He, L.M. Peng, X.Q. Zeng, W.J. Ding, Y.P. Zhu, Mater. Sci. Eng. A 433 (1–2) (2006) 175–181.
[3] J. Zhang, et al., J. Alloys Compd. 464 (1) (2008) 556–564.
[4] X. Gao, S.M. He, X.Q. Zeng, L.M. Peng, W.J. Ding, J.F. Nie, Mater. Sci. Eng. A 431 (1) (2006) 322–327.
[5] T. Honma, T. Ohkubo, K. Hono, S. Kamado, Mater. Sci. Eng. A 395 (1) (2005) 301–306.
[6] J.F. Nie, B.C. Muddle, Acta Mater 48 (8) (2000) 1691–1703.
[7] C. Antion, P. Donnadieu, F. Perrard, A. Deschamps, C. Tassin, A. Pisch, Acta Mater. 51 (18) (2003) 5335–5348.
[8] B. Smola, I. Stulíková, J. Pelcová, B.L. Mordike, J. Alloys Compd. 378 (1) (2004) 196–201.
[9] N.G. Connelly, T. Damhus, R.M. Hartshorn, A.T. Hutton (Eds.), "Nomenclature of Inorganic Chemistry: IUPAC Recommendations 2005 (PDF)." RSC Publ., Cambridge, 2005.
[10] T.E. Leontis, Trans. Metall. Soc. AIME 185 (1949) 327.
[11] Q. Li, Q. Wang, Y. Wang, X. Zeng, W. Ding, J. Alloys Compd. 427 (1) (2007) 115–123.
[12] M. YANG, T. GUO, C. QIN, F. PAN, J. Rare Earths 30 (2) (2012) 181–188.
[13] N. Stanford, D. Atwell, M.R. Barnett, Acta Mater. 58 (20) (2010) 6773–6783.
[14] H. Yu, et al., J. Alloys Compd. 586 (2014) 757–765.
[15] M. Avedesian, H. Baker, ASM Specialty Handbook: Magnesium and Magnesium Alloys, ASM International, 1999.
[16] M.H. Yoo, J.R. Morris, K.M. Ho, S.R. Agnew, Metall. Mater. Trans. A 33 (3) (2002) 813–822.
[17] N. Stanford, M.R. Barnett, Mater. Sci. Eng. A 496 (1) (2008) 399–408.
[18] N. Stanford, M. Barnett, Scr. Mater. 58 (3) (2008) 179–182.
[19] N. Stanford, Mater. Sci. Eng. A 527 (10) (2010) 2669–2677.
[20] K. Hantzsche, J. Bohlen, J. Wendt, K.U. Kainer, S.B. Yi, D. Letzig, Scr. Mater. 63 (7) (2010) 725–730.
[21] L.W.F. Mackenzie, M.O. Pekguleryuz, Scr. Mater. 59 (6) (2008) 665–668.
[22] J. Bohlen, M.R. Nürnberg, J.W. Senn, D. Letzig, S.R. Agnew, Acta Mater. 55 (6) (2007) 2101–2112.
[23] C. Xu, et al., Mater. Sci. Eng. A 559 (2013) 615–622.
[24] R.S. Coelho, A. Kostka, H. Pinto, S. Riekehr, M. Koçak, A.R. Pyzalla, Mater. Sci. Eng. A 485 (1) (2008) 20–30.
[25] D.W. Brown, S.R. Agnew, M.A.M. Bourke, T.M. Holden, S.C. Vogel, C.N. Tomé, Mater. Sci. Eng. A 399 (1) (2005) 1–12.
[26] E.P. Silva, Fundição, laminação e soldagem por fricção e mistura mecânica de ligas de magnésio com adição de Mischmetal. Tese de Doutorado, Escola de Engenharia de São Carlos, Universidade de São Paulo, São Carlos, vol 1, 2016, pp. 1–149, doi:10.11606/T.18.2017.tde-09022017-081216.
[27] M. Ferrari, L. Lutterotti, J. Appl. Phys. 76 (11) (1994) 7246–7255.
[28] H. Okamoto, Desk handbook - Phase Diagram for Binary Alloys, ASM International, 2000.
[29] N.C. Popa, J. Appl. Crystallogr. 31 (2) (1998) 176–180.
[30] W.A. Dollase, J. Appl. Crystallogr. 19 (4) (Aug. 1986) 267–272.
[31] E.P. Silva, L.F. Batista, B. Callegari, R.H. Buzolin, F. Warchomicka, G.C. Requena, P.P. Brito, H.C. Pinto, Mater. Res. 17 (6) (2014) 1507–1512.
[32] E.P. Silva, R.H. Buzolin, B. Callegari, F. Warchomicka, G.C. Requena, H.C. Pinto, Mater. Sci. Forum 879 (2016) 2300–2305.
[33] E.P. Silva, et al., Adv. Mater. Res. 922 (2014) 694–699.
[34] E.P. Silva, F. Marques, T.S. Nossa, U. Alfaro, H.C. Pinto, Mater. Sci. Eng. A 723 (2018) 306–313.
[35] G. Xu, et al., J. Magnes. Alloy. 4 (4) (2016) 249–264.
[36] Z. Zhu, A.D. Pelton, J. Alloys Compd. 652 (2015) 426–443.
[37] M. Birkholz, Thin Film Analysis by X-Ray Scattering, Wiley-VCH Verlag GmbH Co. KGaA, Weinheim, 2006.
[38] B. Warren, X-ray Diffraction, Addison-Wesley, Reading, MA, 1969.
[39] B.D. Cullity, Elements of x-ray Diffraction, 2nd Ed., Addison-Wesley, Mento Park, CA, 1978.
[40] M.G. Moore, W.P. Evans, SAE Trans. 66 (1958) 340–345.
[41] R.A. Poggie, J.J. Wert, Wear 149 (1) (1991) 209–220.
[42] M. Lindgren, T. Lepistö, NDT E Int 34 (5) (2001) 337–344.
[43] M.J. Balart, A. Bouzina, L. Edwards, M.E. Fitzpatrick, Mater. Sci. Eng. A 367 (1) (2004) 132–142.
[44] S. Asgari, E. El-Danaf, S.R. Kalidindi, R.D. Doherty, Metall. Mater. Trans. A 28 (9) (1997) 1781–1795.
[45] A. Rollett, F. Humphreys, G.S. Rohrer, M. Hatherly, Recrystallization and Related Annealing Phenomena: Second Edition, 2nd Ed., Elsevier Ltd, Oxford, 2004.
[46] S.Q. Zhu, S.P. Ringer, Acta Mater. 144 (2018) 365–375.
[47] K. Huang, R.E. Logé, Mater. Design 111 (2016) 548–574.
[48] S. Gourdet, F. Montheillet, Acta Mater. 51 (9) (2003) 2685–2699.
[49] Z.C.C. Sun, H.L.L. Wu, J. Cao, Z.K.K. Yin, Int. J. Plast. 106 (2018) 73–87.
[50] A. Galiyev, R. Kaibyshev, G. Gottstein, Acta Mater. 49 (7) (2001) 1199–1207.

[51] S.M. Fatemi-Varzaneh, A. Zarei-Hanzaki, H. Beladi, Mater. Sci. Eng. A 456 (1) (2007) 52–57.
[52] N.D. Ryan, H.J. McQueen, E. Evangelista, Mater. Sci. Eng. 81 (1986) 259–272.
[53] H. Chen, S.B. Kang, H. Yu, J. Cho, H.W. Kim, G. Min, J. Alloys Compd. 476 (1) (2009) 324–328.
[54] J. Jiang, T. Ben Britton, A.J. Wilkinson, Philos. Mag. Lett. 92 (11) (2012) 580–588.
[55] S. Wulfinghoff, T. Böhlke, Int. J. Plast. 69 (2015) 152–169.
[56] J.D. Robson, D.T. Henry, B. Davis, Acta Mater 57 (9) (2009) 2739–2747.
[57] M. Mabuchi, K. Kubota, K. Higashi, J. Mater. Sci. 31 (6) (1996) 1529–1535.
[58] E.A. Ball, P.B. Prangnell, Scr. Metall. Mater. 31 (2) (1994) 111–116.